Journal of Innovative Optical Health Sciences
Vol. 1, No. 1 (2008) 115–124

World Scientific
www.worldscientific.com

DECOMPOSITION BASED IMAGING WITH FIBER AND CCD CAMERA DETECTIONS

S. D. CAMPBELL, I. L. GOODIN, S. D. GROBE,
Q. SU and R. GROBE

Intense Laser Physics Theory Unit
and Department of Physics
Illinois State University
Normal, IL 61790-4560 USA

We generalize a previously proposed imaging scheme to situations for which the set of hidden objects embedded in the highly scattering medium can take arbitrary shapes. We compare the accuracy of images obtained from optical detection fibers with those from a ccd camera. The latter approach is more efficient and can be applied to non-contact geometries, but it requires an a priori linearization of the obtained digitized images. We discuss some details of this calibration for the camera and establish its potential as a new tool for decomposition based imaging.

1. Introduction to Decomposition Based Imaging

There has been a wide interest in medicine to explore new imaging techniques that are based on laser light illumination.[1–3] From a theoretical viewpoint, the interaction of electromagnetic radiation with heterogeneous biomaterials is complicated and only approximate analytical solutions are available to predict the spectrum or the spatial distribution of the scattered light from the knowledge of the structural composition of the material. The inverse problem of reconstructing the material properties from the features of the scattered light is even more challenging.[4–8]

About a year ago we begun to tackle a less ambitious challenge.[9] Similar as in traditional imaging, the ultimate goal is to be able to recover the structure of objects hidden inside a highly scattering background medium by analyzing the scattered light. However, we treat the forward problem exactly. As a price to pay for this advantage we have to assume some prior knowledge about the system. We examined theoretically and experimentally an imaging scheme that used the transverse intensity profile of the scattered light to reconstruct the locations of several rod-shaped absorbers embedded in a milk-water solution. This method is based on an a priori knowledge of the scattered light patterns associated with a known single absorber that is placed at various positions inside the medium.

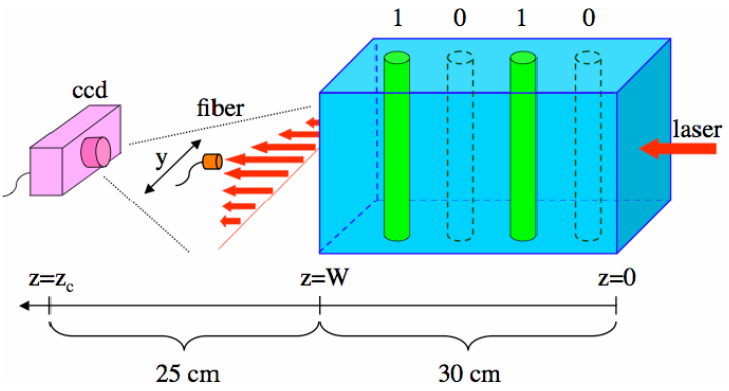

Fig. 1. A sketch of the experimental setup with two rods embedded in the tank. The 12 liter tank has a height of 26 cm and a transverse width of 30 cm. The rods have a diameter of 0.95 cm.

In Fig. 1 we sketch a typical experimental set-up discussed in Refs. 9 and 10. A 80 mW diode laser beam at 661 nm was injected into a tank filled with a water-milk solution as a background scattering medium.[11–13] At the exit surface the brightness distribution $B_{\mathrm{bbbb}}(y)$ of the transmitted light was monitored by an optical fiber that was scanned along the transverse direction (y-axis) with respect to the incoming light. The corresponding four bits in the subscript denote the absence ($b = 0$) or presence ($b = 1$) of an absorbing rod at each of the four possible locations. For example, the particular arrangement shown in the figure corresponds to a two-rod configuration with brightness $B_{1010}(y)$. It turns out that if we are able to measure a priori the corresponding brightness patterns of the four possible single-rod configurations $B_{1000}(y)$, $B_{0100}(y)$, $B_{0010}(y)$ and $B_{0001}(y)$, then one can predict approximately the brightness patterns created by arbitrary arrangements of two, three or four rods. These brightness patterns themselves are not directly related to each other, however, the corresponding shadow functions, defined by subtracting out the zero-rod background light, $S_{\mathrm{bbbb}}(y) \equiv B_{0000}(y) - B_{\mathrm{bbbb}}(y)$, are approximately linearly related to each other. For example, the shadow pattern associated with the two-rod configuration $S_{1010}(y)$ can be remarkably similar to the simple sum of the fourth and second single-rod shadows, $\lambda_4 S_{1000}(y) + \lambda_2 S_{0010}(y)$, with appropriate weight factors λ_4 and λ_2.

In Ref. 9 we have examined this quasi-linearity to reconstruct the relevant weight factors λ_1, λ_2, λ_3 and λ_4 from the shadow pattern of an unknown multi-rod configuration using a multi-regression for a wide range of scattering materials. In a follow-up work[10] we discussed the range of validity of this method, its sensitivity with regard to noise and proposed an algorithm to improve its accuracy.

This decomposition based imaging (dbi) reconstruction scheme was based on the fact that the corresponding shadow patterns as a function of the single scanning parameter y are distinctly different from each other and contain sufficient characteristics of the underlying shadows associated with each rod individually. As a result,

a multi-rod shadow pattern can be decomposed approximately into the weighted sum of the corresponding single-rod shadows.

The original measurements were time consuming, as a single detection fiber had to be scanned mechanically by a stepper motor along the y-axis. In order to make the recording of the measurement data more efficient, one could use a linear array of detection fibers instead. However, for more general situations in which the absorbers are not simple cylindrically symmetric rods but objects with no simplifying geometry, a two dimensional array of fibers would be required. This could become impractical for situations where the exit surfaces of the media to be imaged have different shapes or sizes. For reasons of detection efficiency all previous data[9,10] were taken for a fiber that was placed closer than 1mm to the exit surface of the tank. To obtain an image for a large two dimensional exit surface would almost certainly require a non-contact geometry, a task that would be rather problematic with a detection scheme based on fibers.

One of the long-term goals in decomposition based imaging is the real time imaging of objects that are moving inside the medium. This challenge would require a nearly instant data acquisition accompanied by a fast numerical inversion.

In this note we examine the question whether this decomposition based imaging technique can be applied to general situations where direct light detection at the surface of the medium is not possible. The general question about the detection of scattered light from a diffusive medium in a non-contact geometry has been studied in Refs. 14 and 15. The authors presented a theoretical approach for modeling the intensity distribution from an arbitrarily shaped turbid volume by considering diffuse light propagation in free space and validated it with experiments for a diffusive volume of known geometry in a non-contact situation, both with and without the presence of an embedded absorber.

We will demonstrate in this work the validity of the dbi technique with transmission profiles detected as far as 25 cm from the scattering medium. Due to the small numerical apertures, optical fibers would be unsuited for this task and we have examined the use of a ccd-camera instead.[16] Simple charged-coupled devices have become extremely useful tools in optical imaging[17,18] and spectroscopy.[19] As noted above the dbi is based on the quasi-linearity among the shadow functions. For less expensive devices, however, the value of the recorded pixel value of a digitized image is not always linear to the applied brightness. In order to generate reliable images for dbi, the ccd needs to be calibrated (linearized) first.

2. Calibration of the ccd Device

In order to have a situation similar to Fig. 1 for our calibration, we have computed the brightness pattern associated with a laser beam that has been diffusively widened by scattering medium. As a scattering medium we used a 2% milk-water mixture with a concentration of 100 ml 2% fat milk in 9.2 l water. This suggests[12] a

scattering coefficient of about $\mu_s = 3.3\,\mathrm{cm}^{-1}$ leading to an inverse scattering length of about 0.3 cm.

The goal is to find the universal function $P = F(p)$ for our laser wavelength that maps the original pixel height p (which in a typical 8-bit environment ranges from $p = 0$ to $p = 255$) into a scaled pixel height P that scales linearly with the incident laser intensity. In order to create such a look-up table, we used a beam splitter to create a reference beam that was fed into a broad area photo detector (NewFocus 2031) whose output voltage scales rather linear with the laser intensity. Using several filters and also the electric current control of the diode laser we created twelve input intensities, associated with the photo detector voltages V_n (with $n = 1, 2, \ldots, N_V = 12$ and $V_n = 0.153$, 0.360, 0.456, 0.662, 0.885, 0.990, 1.130, 1.770, 1.835, 2.280, 2.660 and 2.770 volts).

As a ccd camera we used an inexpensive cmos-based Dynex DX-DTCAM with Iris software which has a 300 K resolution of 640×480 pixels. The camera was placed about 25 cm behind the exit surface of the tank and imaged an area of about 15 cm × 11 cm. This means that the resolution corresponds to an area of about 0.23 mm × 0.23 mm per single pixel.

For each of the twelve intensities V_n, we recorded 150 frames during a 30 second period. Using the NIH software package ImageJ,[20] we averaged the 150 frames in order to reduce the temporally fluctuating patterns. The typical standard deviation in time for each pixel was typically in the range of $\Delta p = 3$. We denote the pixel heights in these twelve temporally averaged frames with $p(x, y; V_n)$. In order to maximize the information contained in each frame we have defined $N_R = 64$ different non-overlapping regions of interest of 5×5 pixels each. The jth region ($j = 1, 2, \ldots, N_R$) contains the 25 pixels located inside the square $[5(j-1) \le x < 5j$, $239 \le y < 244]$. The size of each region was small enough such that the 25 pixel heights differed from each other by less than $\Delta p = 1$; while at the same time it was large enough to average out any unwanted fluctuations. We denote the average pixel height of the jth region by $q(j; V_n) \equiv \langle p(x, y; V_n)\rangle_j$.

The spatial brightness profile of the covered 15 cm × 11 cm area is linearly proportional to the voltage V_n measured at the photo detector, $B(x, y; V_n) = V_n u(x, y)$. Here we denote with $u(x, y)$ the normalized spatial laser profile. Its average value in the jth region is denoted by $u(j) \equiv \langle u(x, y)\rangle_j$. For each region the height q is a nonlinear function of the brightness, $q(j; V_n) = G[B(x, y; V_n)]$. If we assume that q grows monotonically with B, the inverse function can be defined, $B = G^{-1}[q]$. In other words, we have $V_n = [1/u(j)]G^{-1}[q(j; V_n)]$. As a result, the N_R curves graphing the voltage as a function of the regions' pixel height differ by a simple multiplicative factor related to the normalized average laser profile, $u(j)$.

In order to combine the information contained in each of these N_R curves into a single one, the factor $u(j)$ needs to be extracted out. We want to take many measured data points into account for this normalization, so we required of all curves to have the same area independent of j. This corresponds to multiplying a

factor to V_n to find $\nu(j)[1/u(j)]G^{-1}[q(j;V_n)]$ where $\nu(j)^{-1} \equiv \int dq V_n(q_j)$. As each curve was defined by only N_V different data points, we computed the 6th order interpolating polynomial for each curve and integrated this analytically from $q_{\min}$ to $q_{\max}$. These boundaries had to be chosen inside each of the curves, corresponding to $q_{\min} = 20$ and $q_{\max} = 92$ for our case.

As a last step, we normalized the resulting set of data points to map the pixel number $q = 50$ into a voltage of 50 V, introducing a scaling factor α to produce the normalized pixel height $P \equiv \alpha\nu(j)[1/u(j)]G^{-1}[q(j;V_n)]$. This rescaled voltage corresponds to the ideal pixel height a perfectly linear ccd camera should indicate. In other words, the resulting appropriately normalized numerical curve, $P = F(p) \equiv \alpha\nu(j)[1/u(j)]G^{-1}[q(j;V_n)]$ is our calibration curve, where we set $p = q$.

In Fig. 2 we show the obtained rescaled pixel height P as a function of the original pixel height p, graphed for the $N_R N_V$ $(= 12 \times 64)$ data points. Several observations are in order. First of all, the fact that the $N_R N_V$ points from different regions align relatively well along a single curve is encouraging and suggests that it is possible to define a universal curve that describes an un-ambiguous mapping of the pixel height to the laser brightness. This suggests that each pixel responds in a similar way to the local laser intensity. We also see deviations from the linear behavior for very small pixel values. As a result, the curve does not go exactly through the origin $(P, p) = (0, 0)$. This could be related to dark currents of the camera such that pixel heights below 10 are not very accurate. In the next region from $p = 10$ to $p = 80$ the data agree very well with the dashed line $P = p$ that we have included for comparison. This is the regime in which the camera responds linearly to the light and a calibration would not be necessary. For pixel values larger than 80, however, we note the saturation to set in. A doubling of the laser intensity

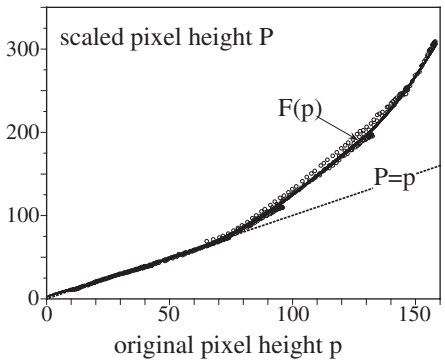

Fig. 2. The scaled pixel height P as a function of the original value detected by the ccd camera obtained from $N_V = 12$ different brightnesses. Each frame was divided into $N_R = 64$ different regions of interest with a size of 5×5 pixels. The solid curve is the 8th order fitting polynomial $P = F(p) = \sum_{k=0}^{8} C_k p^k$ with the coefficients, $C_0 = 4.3142$, $C_1 = 0.63601$, $C_2 = 5.6089 \times 10^{-3}$, $C_3 = 6.7355 \times 10^{-4}$, $C_4 = -3.5251 \times 10^{-5}$, $C_5 = 6.8436 \times 10^{-7}$, $C_6 = -6.3121 \times 10^{-9}$, $C_7 = 2.8076 \times 10^{-11}$ and $C_8 = -4.8431 \times 10^{-14}$. To judge the amount of saturation, we have also included the dashed line $P = p$.

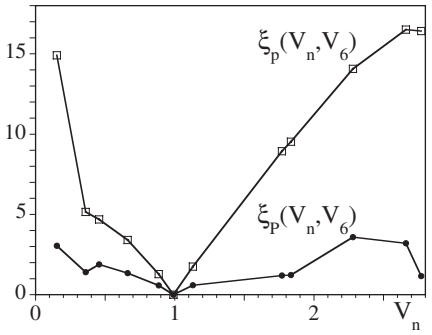

Fig. 3. The quality of the calibration curve shown in Fig. 2. The parameter $\xi_p\ (V_n, V_6)$ compares average difference in pixel height of $p(x, y; V_6)/V_6$ with the pixel values obtained from 11 other brightnesses. The lower curve shows this average difference for the frames that were recalibrated, $P(x, y; V_n)/V_n$ using $P = F(p)$.

no longer leads to a doubling of the pixel height. In fact, a brightness leading with our camera to a pixel value of $p = 150$ would correspond in an ideal camera to a value of $P = 275$ as can be read off the graph. This collection of $N_R N_V$ data can now be used as a look-up table to recalibrate our camera in order to compensate for saturation and other nonlinear effects.

In order to have an analytical function $P = F(p)$ that describes this calibration we have used a 8th order polynomial fitting curve. We have also included this graph into the figure. As a side issue, we should mention that we have repeated the same analysis for usual incandescent light bulbs of various brightness. We found that in contrast to the graph $P = F(p)$ for the monochromatic case, the curve differed significantly for $p > 80$, illustrating the expected result that the saturation behavior does depend strongly on the frequency of the detected light.

In order to be able to judge the amount of improvement of this calibration scheme, we have first taken our N_V original frames (with uncalibrated pixel values) and divided each height by the voltage of the corresponding frame, $p(x, y; V_n)/V_n$. If the camera were perfectly linear, the resulting frames should be completely identical. To measure this quantitatively, the average difference in pixel height was defined as

$$\xi_p(V_n, V_m) \equiv \langle |p(x, y; V_n)/V_n - p(x, y; V_m)/V_m| \rangle_{x,y} \tag{2.1}$$

where $\langle \ldots \rangle_{x,y}$ denotes the average over all 640×480 pixels. This parameter $\xi_p(V_n, V_m)$ should vanish identically for an ideal camera as it characterizes the average degree of nonlinearity for the response to two different laser illuminations.

As a numerical example we illustrate this nonlinearity relative to the measurement with the laser brightness associated with $V_{m=6} = 0.99$ Volt. While frames associated with similar voltages differ on average by only a few pixel values, the average difference for the frames for $V_1\ (= 0.153V)$ and V_6 is about 15. This difference is very large (26%) considering the fact that the average pixel height for

$p(x, y; V_6)/V_6$ is about 58. The lower lying curve $\xi_P(V_n, V_6)$ is obtained from the frames, where each single pixel was rescaled according to the 8th order polynomial fit $P = \sum_{k=0}^{8} C_k p^k$. The values of the nine expansion coefficients are given in the Figure caption 2. It is clear that the recalibration is not perfect but reduces the nonlinearity to a ξ-value less than 4.

3. Two Dimensional dbi

Except for the different method of light detection, the experimental setup we used is identical to that of previous works so we can refer the reader to the detailed accounts in Refs. 9, 10. As mentioned in the introduction, we placed a single rod at each of the four locations and using the ccd camera we measured the corresponding brightness patterns denoted by $B_{1000}(x, y)$, $B_{0100}(x, y)$, $B_{0010}(x, y)$, and $B_{0001}(x, y)$. Together with $B_{0000}(x, y)$, these patterns were used to compute the corresponding four shadows functions. An example of the resulting images and shadow patterns for the particular two-rod configuration $B_{1010}(x, y)$ is shown in Fig. 4. In order to see the effect of the calibration of each pixel, we have included in the bottom row graphs of the pixel heights along the line $y = 239$ before and after the calibration. It is clear that the calibration changes the shadow shapes significantly.

We have measured the scattered light for the remaining eleven different arrangements possible for our system with a maximum of four absorbers. These include six

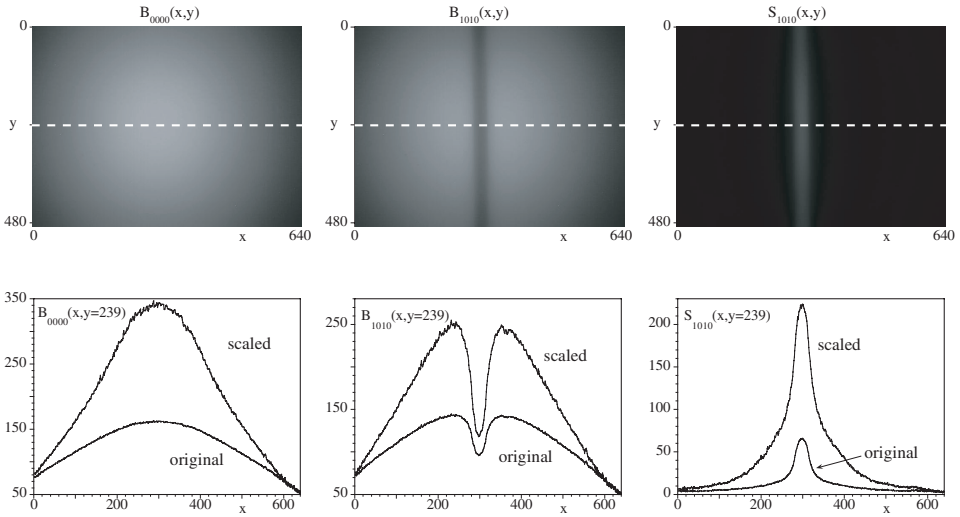

Fig. 4. The top row shows the brightness patterns for the background scattering medium, $B_{0000}(x, y)$ and a two-rod combination, $B_{1010}(x, y)$, together with the corresponding shadow distribution, $S_{1010}(x, y)$. The bottom row shows the pixel height of the patterns for all 640 pixels along the horizontal line $y = 239$. The upper curve shows the effect of the recalibration based on the curve in Fig. 2. [The experimental set up and parameters were identical to those in Ref. 10.]

2-rod configurations (1100, 1010, 1001, 0110, 0101 and 0011), four 3-rod configurations (1110, 1101, 1011 and 0111) and finally one 4-rod configuration (1111).

We then used a multi-regression analysis to decompose each of the multi-rod data into a superposition of the single rods with unknown weight factors λ_n. For brevity, we denote these four single-rod (calibration) states by $\sigma_n(x, y)$, with $n = 1, \ldots, 4$. The goal in the DBI method is to express each of the eleven multi-rod shadow patterns approximately as an arithmetic sum of the four calibration states with optimum weight factors λ_n. The decomposition was done by using the standard χ^2 linear least square fitting approach,[21] where the factors λ_n were determined from minimizing the error between the particular shadow signal $S_{\mathrm{bbbb}}(x, y)$ and the superposition of the four single-rod states

$$\chi^2\{\lambda_n\} \equiv \iint dxdy \left[S_{bbbb}(x, y) - \sum_{n=1}^{4} \lambda_n \sigma_n(x, y) \right]^2 \tag{3.1}$$

The resulting four linear equations for the weights λ_n can be obtained from the four conditions $\partial\chi^2/\partial\lambda_n = 0$. The four weights λ_n are obtained by a simple matrix inversion.

Table 1 shows the resulting weight factors λ_n for the experimental data. For a better comparison, the digits in the parentheses indicate the presence (1) or absence (0) of an absorber. We note that some configurations require negative weights or weights with absolute values larger than unity in order to best approximate the image obtained from the multiple absorbers. For example, the decomposition of the two-absorber shadow $S_{1100}(y)$ (first row of the Table 1) leads to $\lambda_2 = 0.458$ and $\lambda_1 = -0.167$, even though there were no rods at these locations.

Table 1. Weight factors for the experimental data.

λ_4	λ_3	λ_2	λ_1
0.620 (1)	0.715 (1)	0.458 (0)	−0.167 (0)
0.741 (1)	0.033 (0)	0.736 (1)	0.194 (0)
0.796 (1)	−0.201 (0)	0.197 (0)	0.961 (1)
−0.011 (0)	0.634 (1)	0.655 (1)	0.298 (0)
0.023 (0)	0.532 (1)	0.112 (0)	1.019 (1)
0.009 (0)	0.025 (0)	0.187 (1)	1.309 (1)
0.548 (1)	0.357 (1)	0.940 (1)	0.251 (0)
0.569 (1)	0.224 (1)	0.435 (0)	0.961 (1)
0.699 (1)	−0.273 (0)	0.442 (1)	1.271 (1)
0.025 (0)	0.372 (1)	0.142 (1)	1.460 (1)
0.534 (1)	0.015 (1)	0.579 (1)	1.332 (1)

Note: The weight factors λ_1, λ_2, λ_3 and λ_4 associated with the shadow basis states S_{0001}, S_{0010}, S_{0100} and S_{1000} for eleven different absorber combinations. The presence/absence of an absorber in the experiment is indicated by the number in the parenthesis.

We see that our preliminary data are not perfect. However, the data are encouraging in the sense that the corresponding Tables reported in Ref. 10 are of comparable quality. This certainly suggests that changing from an inefficient on-contact geometry to two-dimensional images obtained from ccd cameras does not necessarily deteriorate the image or the inversion quality significantly.

To have a more quantitative comparison for the accuracy of the reconstruction scheme we have introduced in[10] a parameter C. It is based on the assumption that a single-rod state associated with a rod that is absent in the multi-rod configuration should have ideally a vanishing weight in the superposition. In our signal space of eleven multi-rod configurations with a total of 44 weights factors, 16 weights correspond to an absent rod indicated by (0). We therefore define a contamination factor C as the average of the (absolute value) of all those 16 weight factors, that correspond to an absent rod. For our experimental data in the Table, this amounts to $C = 0.17$. This value is sufficiently close enough to zero that the identification of the non-existent rods should be possible. For comparison, we obtained a comparable value of $C = 0.13$ from the one-dimensional images obtained from the detection with an optical fiber.

In summary, we have reported on the first dbi data that are based on images obtained from a ccd camera. This situation for a non-contact geometry required a linearization of the images. Our preliminary data suggest that the inversion data can be of comparable quality as those obtained from a single fiber. The fact that now the images can be obtained nearly instantly opens the study to apply dbi techniques to examine real time imaging of a set of moving objects with possible direct applications to bio-optical imaging.

Acknowledgements

We thank Prof. P. Yu (U. Missouri, Columbia) for the loan of special fibers and extremely valuable discussions about ccd cameras during his visit to ILP. We also thank Prof. R. Bogue for numerical help and Profs. G. H. Rutherford and D. Marx for advice. This work has been supported by the NSF. We also acknowledge support from Research Corporation for Cottrell Science Awards and BLV.

References

1. V. V. Tuchin, "Light scattering study of tissues", *Physics* **40**(5), 495 (1997).
2. J. T. Bushberg, J. A. Seibert, E. M. Leidholdt, Jr. and J. M. Boone, eds, *The Essential Physics of Medical Imaging*, 2nd ed. (Lippincott Williams & Wilkins, Philadelphia, 2002).
3. S. R. Arridge, "Optical tomography in medical imaging", *Inverse Problems* 15, R41 (1999).
4. E. P. Zege, A. P. Ivanov and I. L. Katsev, *Image Transfer through a Scattering Medium* (Springer Verlag, Berlin, 1991).
5. G. M. L. Gladwell, *Inverse Problems in Scattering* (Kluwer Academic Publishers, Dordrecht, 1993).

6. M. A. O'Leary, D. A. Boas, B. Chance and A. G. Yodh, "Fluorescence lifetime imaging in turbid media", *Opt. Lett.* **21**, 158 (1996).
7. O. Dorn, "A transport-backtransport method for optical tomography", *Inverse Problems* **14**, 1107 (1998).
8. For a special issue on diffusive imaging, see Optics Express, Vol. 4, No. 8 (1999).
9. S. D. Campbell, I. L. Goodin, S. D. Grobe, Q. Su and R. Grobe, "Decomposition based recovery of absorbers in turbid media", *Phys. Rev. A* **76**, 063802 (2007).
10. S. D. Campbell, S. D. Grobe, I. L. Goodin, Q. Su and R. Grobe, "Limitations of decomposition based imaging of longitudinal absorber configurations", *Phys. Rev. A* **77**, 023821 (2008).
11. S. Campbell, A. M. O'Connell, S. Menon, Q. Su and R. Grobe, "Light scattering regimes along the optical axis in turbid media", *Phys. Rev. E* **74**, 061909 (2006).
12. S. Campbell, S. Menon, Q. Su, G. H. Rutherford and R. Grobe, "Scaling of light-scattering with density of scatterers", *Las. Phys.* **17**, 117 (2007).
13. S. Campbell, A. M. O'Connell, G. H. Rutherford and R. Grobe, "Impact of large-angle scattering on diffusively backscattered halos", *Opt. Lett.* **32**, 560 (2007).
14. J. Ripoll, R. B. Schulz and V. Ntziachristos, "Free-space propagation of diffuse light: theory and experiments", *Phys. Rev. Lett.* **91**, 103901 (2003).
15. R. B. Schulz, J. Ripoll and V. Ntziachristos, "Noncontact optical tomography of turbid media", *Opt. Lett.* **28**, 1701 (2003).
16. C. Pollak and H. Hutter, "A webcam as a recording device for light microscopes", *J. Comp. Assist. Microsc.* **10**, 179 (1998).
17. C. de Izarra and O. Vallee, "On the use of linear CCD image sensors in optics experiments", *Am. J. Phys.* **62**, 357 (1994).
18. M. Vannoni and G. Molesini, "Speckle interferometry experiments with a digital camera", *Am. J. Phys.* **72**, 906 (2004).
19. C. Lengacher, S. Macklin, D. Hite and M. F. Masters, "Low cost CCD detectors for spectroscopy", *Am. J. Phys.* **66**, 1025 (1998).
20. Image J is an excellent image processing software that is provided by the National Institute of Health, see http://rsb.info.nih.gov/ij/
21. See, e.g., R. C. Aster, B. Borchers and C. H. Thurber, *Parameter Estimation and Inverse Problems* (Elsevier Academic Press, Amsterdam, 2005).